Microstructure-based finite deformation modelling of super-elastic NiTi shape memory alloy considering various inelastic mechanisms

Parvin Ebrahimi[a,b] , Jamal Arghavani[a] , Saeed Sohrabpour[a], J. Patrick McGarry[b,*], Reza Naghdabadi[a,c,*]

[a]Mechanical engineering department, Sharif University of Technology, Tehran, Iran

[b]School of Engineering, National University of Ireland Galway, Ireland

[c]Institute for Nano-Science and Technology, Sharif University of Technology, Tehran, Iran

Abstract

In this study the mechanisms of transformation-induced plasticity (TRIP), detwinning-induced plasticity (DIP), and accumulation of residual martensite, are incorporated into a finite-deformation crystal plasticity model of NiTi SMA for the first time. The constitutive model is constructed at the single-crystal scale and also includes phase transformation and detwinning mechanisms. Using a proposed Helmholtz free energy, the driving forces for inelastic mechanisms are derived within the framework of thermodynamics. The constitutive model has been implemented in the Abaqus/Explicit finite-element program, using VUMAT subroutine to simulate a polycrystalline material. Considering various orientations for crystals, the effect of texture on tension-compression asymmetry is investigated. It is shown that different textures may cause stiffer, softer, or similar response in compression compared to tension. Due to the incorporation of the effect of residual martensite, the model provides accurate predictions of experimentally measured residual strain. The incorporation of the aforementioned inelastic deformation mechanisms is shown to accurately capture the key features related to cyclic loading. Finally, the effect of detwinning-induced plasticity in compressive cyclic loading of NiTi SMA is investigated. In strain-controlled cyclic compression-unloading tests DIP leads to a less negative peak stress and a more negative residual strain following several loading cycles.

Keywords: NiTi; Detwining-induced plasticity; Constitutive modeling; Crystal plasticity

* Corresponding authors: patrick.mcgarry@nuigalway.ie, naghdabd@sharif.edu

1. Introduction

Shape memory alloys (SMAs), due to unique characteristics such as super-elasticity and shape memory effect, are used for a range of applications, including biomedical devices [1,2], robotics [3,4], aerospace [5], actuators [6], and automotive structures [7]. NiTi is the most widely used SMA due to its high energy density, corrosion resistance, and biocompatibility [1,5].

The behavior of NiTi SMA is based on the temperature-dependent reversible phase transformation from the high symmetry austenite phase to the low symmetry martensite phase and vice versa [8]. At temperatures higher than the austenite finish-temperature, application of stress to austenite will cause strain generation, which is recoverable upon unloading (super-elasticity). Upon cooling, in the absence of stress, the high temperature austenite phase will transform to the low temperature martensite phase (austenite to twinned-martensite transformation). Application of enough stress to twinned-martensite will cause strain generation during loading, which is not recovered upon unloading, and requires subsequent heating to be recovered (shape-memory effect).

Many constitutive models have been developed to predict the behavior of SMAs based on experimental observations. The models can be categorized into two main groups: macroscopic phenomenological models and microstructure-based models. Typical macroscopic constitutive models include Auricchio et al. [9], Lagoudas et al. [10], Panico and Brinson [11], Zaki and Moumni [12], Arghavani et al. [13], and Xu et al. [14]. While macroscopic models do not consider the microscale mechanisms underlying SMA behavior, they are readily implementable in finite element codes for structural analysis and design.

Microstructure-based constitutive models have been proposed to incorporate the underlying microscale physical mechanisms underlying SMA behavior. Among them, microstructure-based models based on crystal plasticity formulation are popular since various martensite variants with different morphological features and their evolution laws during deformation can be incorporated into such a framework. These models are developed at the single-crystal scale and then, adopting finite element method or scale-transition rules, transformed to the poly-crystal scale. Representative constitutive models include Thamburaja and Anand [15–17], Anand and Gurtin [18], Thamburaja [19], Thamburaja et al. [20], Wang et al. [21], Manchiraju and Anderson [22], Yu et al. [23–26], Xiao et al. [27], and Dhala et al. [28]. It should be noted that some of the above-mentioned constitutive models do not consider the effect of large

deformations in the modeling framework. In practical applications, the strains and rotations applied to SMA can be quite large such that the theories of small deformation cannot be used to reasonably predict the behavior of these materials. In recent years, the behavior of NiTi SMAs under finite deformations has been studied by some researchers. The effect of phase transformation on the mechanical and thermomechanical response of NiTi SMA has been investigated by Thamburaja and Anand [15–17], and Anand and Gurtin [18]. The effects of detwinning and reorientation have been incorporated into constitutive modeling of NiTi SMA by Thamburaja [19]. This model has been modified to consider austenite to martensite phase transformation, as well [20]. Manchiraju and Anderson [22] considered the effects of phase transformation and austenite plasticity, which results from phase transformation at high temperatures. It should be noted that the residual strain observed in this modeling is due to austenite plasticity, occurs only at sufficiently high temperatures, and differs from the mechanism associated with the accumulation of residual martensite, which can be activated at any temperature. The effects of austenite-plasticity and martensite-plasticity on the mechanical behavior of super-elastic NiTi have been investigated by Dhala et al. [28]. During phase transformation, some martensite variants are locked, due to increase of defects, and cannot return to austenite phase. This process, called accumulation of residual martensite, is known to be one of the main mechanisms in the deformation of super-elastic NiTi SMA [25,29]. It should be noted that the effect of residual martensite has not been considered in the above-mentioned finite deformation constitutive models, while it is evident in experimental observations. On the other hand, some kind of plasticity can be activated in SMAs even when the applied stress is much lower than the yield stress of austenite and martensite phases [8]. Due to misfit at the interfaces of austenite and different variants of martensite, a local stress field will be induced in these areas [30]. The plastic deformation which is created to overcome this local stress field is called transformation-induced plasticity [23], which has significant effect on predicting the behavior of NiTi SMA under cyclic loading [8]. In addition, the experimental results of Liu et al. [31] show a high density of dislocations at the interfaces of lattice correspondent variants during compressive loading, but no significant plastic deformation is detected in such areas under tension. The irrecoverable strain which is induced to relax the local stress field at the interfaces of lattice correspondent variants is referred to as detwinning-induced plasticity (DIP) [32]. As demonstrated by Ebrahimi et al. [32], DIP has considerable effect on compressive cyclic loading of NiTi SMAs. It should be noted that the cyclic behavior of NiTi SMA, considering the crucial mechanisms of TRIP and DIP, has not been investigated in previous studies.

The goal of the current study is to predict the behavior of NiTi under monotonic and cyclic loadings considering large deformations. Using crystal plasticity formulation, diverse mechanisms of phase transformation, transformation-induced plasticity, detwinning, detwinning-induced plasticity, and accumulation of residual martensite have been incorporated into finite-deformation modeling of NiTi SMA. The single-crystal constitutive model has been implemented in the Abaqus/Explicit finite-element program, using VUMAT subroutine to obtain the polycrystalline response. The model is shown to capture various features observed during monotonic and cyclic loading of super-elastic NiTi.

2. Micromechanical constitutive model

2.1. Single crystal constitutive model in the framework of thermodynamics

Using polar decomposition theorem, the deformation gradient tensor $\mathbf{F}$ can be decomposed into elastic, $\mathbf{F}^e$, and inelastic, $\mathbf{F}^p$, parts [19,33]:

$$\mathbf{F} = \mathbf{F}^e\mathbf{F}^p \tag{1}$$

where $\mathbf{F}^p$ is composed of several parts related to different mechanisms of phase transformation (tr), detwinning (det), transformation-induced plasticity (TRIP), and detwinning-induced plasticity (DIP).

The velocity gradient tensor, $\mathbf{L}$, can also be divided into elastic, $\mathbf{L}^e$, and inelastic, $\mathbf{L}^p$, parts [28,34,35]:

$$\mathbf{L} = \dot{\mathbf{F}}\mathbf{F}^{-1} = (\dot{\mathbf{F}}^e\mathbf{F}^p + \mathbf{F}^e\dot{\mathbf{F}}^p)(\mathbf{F}^{p^{-1}}\mathbf{F}^{e^{-1}}) = \dot{\mathbf{F}}^e\mathbf{F}^{e^{-1}} + \mathbf{F}^e\dot{\mathbf{F}}^p\mathbf{F}^{p^{-1}}\mathbf{F}^{e^{-1}} \tag{2}$$

$$\mathbf{L}^e = \dot{\mathbf{F}}^e\mathbf{F}^{e^{-1}}, \qquad \mathbf{L}^p = \dot{\mathbf{F}}^p\mathbf{F}^{p^{-1}} \tag{3}$$

The plastic velocity gradient tensor, $\mathbf{L}^p$, comprises various velocity gradient tensors related to phase transformation $\mathbf{L}^{tr}$, transformation-induced plasticity $\mathbf{L}^{TRIP}$, detwinning $\mathbf{L}^{\det}$, and detwinning-induced plasticity $\mathbf{L}^{DIP}$.

Accumulation of residual martensite causes the volume fraction of each martensite variant to be divided into the reversible martensite volume fraction ξ^{α}_{rev} and the irreversible (residual) martensite volume fraction ξ^{α}_{ire}. The total volume fraction of martensite is obtained by summing the reversible and irreversible parts of each variant:

$$\xi^{\alpha} = \xi^{\alpha}_{rev} + \xi^{\alpha}_{ire} \tag{4}$$

$$\xi = \sum_{\alpha=1}^{24} \xi^{\alpha}, \qquad \xi_{rev} = \sum_{\alpha=1}^{24} \xi^{\alpha}_{rev}, \qquad \xi_{ire} = \sum_{\alpha=1}^{24} \xi^{\alpha}_{ire} \tag{5}$$

where ξ, ξ_{rev}, and ξ_{ire} are the total, reversible, and irreversible martensite volume fractions, respectively. ξ^{α} is the martensite volume fraction for the α-th martensite variant.

The orientation tensor $\mathbf{P}^{\alpha}$ of the α-th martensite variant which is related to the transformation direction $\mathbf{b}^{\alpha}$, and the habit plane normal $\mathbf{m}^{\alpha}$, of the α-th martensite variant, can be expressed by [15,18]:

$$\mathbf{P}^{\alpha} = \mathbf{b}^{\alpha} \otimes \mathbf{m}^{\alpha} \tag{6}$$

The magnitudes of habit plane normal $\mathbf{b}^{\alpha}$ and transformation direction $\mathbf{m}^{\alpha}$ of 24 variants are listed in the Appendix.

By reducing the temperature to a value lower than the martensite finish-temperature, austenite will transform to martensite in the absence of stress. The martensitic plates or habit plane variants (HPVs) that form due to phase transformation, comprises two lattice correspondent variants (LCVs), which are called sub-variants [24,32]. The movement of interfaces between LCVs, which is motivated by the application of stress, is referred to as detwinning [19]. The orientation tensor for the α-th detwinning system, $\mathbf{P}^{\alpha}_{det}$, which is related to shear direction for detwinning $\mathbf{a}^{\alpha}$, and unit vector normal to detwinning plane $\mathbf{w}^{\alpha}$, of the α-th martensite variant is such that:

$$\mathbf{P}^{\alpha}_{\mathrm{det}} = \mathbf{a}^{\alpha} \otimes \mathbf{w}^{\alpha} \tag{7}$$

The crystallographic data for different detwinning systems are listed in the Appendix.

According to crystal plasticity [20,28,36], the inelastic velocity gradient tensor is proposed here such that:

$$\mathbf{L}^{P} = \dot{\mathbf{F}}^{p}\mathbf{F}^{p^{-1}} = \sum_{\alpha=1}^{24} \dot{\xi}^{\alpha}_{rev} g^{tr}\mathbf{P}^{\alpha} + \sum_{\alpha=1}^{24} \dot{\xi}^{\alpha}_{ire} g^{tr}\mathbf{P}^{\alpha} + \sum_{\alpha=1}^{24} \dot{\gamma}^{\alpha}_{TRIP}\mathbf{P}^{\alpha} + \sum_{\alpha=1}^{24} \dot{\lambda}^{\alpha}\xi^{\alpha}\mathbf{P}^{\alpha}_{\mathrm{det}} + \sum_{\alpha=1}^{24} \dot{\gamma}^{\alpha}_{DIP}\mathbf{P}^{\alpha}_{\mathrm{det}} \tag{8}$$

The terms on the right-hand side of Eq. (8) are related to reversible martensite phase transformation, residual martensite, transformation-induced plasticity, detwinning, and detwinning-induced plasticity, respectively. g^{tr} is the magnitude of shearing deformation

caused by martensite transformation, γ_{TRIP}^{α} is the amount of slipping caused by transformation-induced plasticity at the interface of austenite and the α-th martensite variant, and γ_{DIP}^{α} is the amount of shearing deformation caused by detwinning-induced plasticity in the α-th martensite variant. The volume fractions of two sub-variants in the α-th martensite variant are denoted by λ^{α} and $1-\lambda^{\alpha}$, therefore $\dot{\lambda}^{\alpha}$ represents the amount transformed from one sub-variant to the other. Since TRIP occurs along austenite-martensite interfaces, it is assumed that the orientation tensors for phase transformation and transformation-induced plasticity are the same and the number of friction systems is equal to that of martensite variants [23,25].

Considering a representative volume element (RVE), the Helmholtz free energy can be expressed by:

$$\psi = \psi^{e} + \psi^{ch} + \psi^{\text{int}} + \psi_{rev}^{tr} \tag{9}$$

where ψ^{e} represents the elastic energy of RVE, ψ^{ch} is the chemical energy of RVE, ψ^{int} is the part of free energy reflecting the effect of internal stress, and ψ_{rev}^{tr} is related to the effects of hardening or softening during phase transformation.

The elastic part of free energy can be expressed by [23]:

$$\psi^{e}(\mathbf{E}^{e},\xi) = \frac{1}{2}\mathbf{E}^{e}.(\mathbb{C}(\xi)\mathbf{E}^{e}) \tag{10}$$

where $\mathbb{C}(\xi)$ is the fourth-order elasticity tensor, considered as a function of the volume fraction of martensite according to the law of mixtures, $\mathbb{C} = \mathbb{C}_{A}(1-\xi) + \mathbb{C}_{M}\xi$. $\mathbf{E}^{e}$ is the Green-Lagrange elastic strain tensor.

The chemical energy reflects the effect of ambient temperature on the transformation [19]:

$$\psi^{ch}(\theta,\xi) = \frac{h_T}{\theta_T}(\theta - \theta_T)\xi \tag{11}$$

h_T is the latent heat per unit reference volume which is absorbed or released during phase transformation at the phase equilibrium temperature, θ_T. The phase equilibrium temperature is the temperature at which the free energies of the austenite and martensite phases are equal.

As experimentally observed, the start stress of phase transformation will decrease with increasing number of cycles [29]. ψ^{int} is the part of free energy which reflects the effect of

internal stress [23]. Any reduction in ψ^{int} during cyclic loading will cause a decrease in start stress of phase transformation. Considering the work of Yu et al. [23], the form of ψ^{int} is proposed here such that:

$$\dot{\psi}^{\text{int}} = -\mathbf{B} : \mathbf{L}^{P} \tag{12}$$

$\mathbf{B}$ is an internal variable, known as internal stress, used to consider the effect of stresses caused by phase transformation and detwinning on the overall behavior of the material. The internal stress facilitates the start of transformation and therefore decreases the start-stress of phase transformation.

ψ_{rev}^{tr} reflects the effects of hardening or softening during phase transformation. If ψ_{rev}^{tr} increases, hardening and if it decreases, softening is observed in the behavior of shape memory alloy [23].

$$\dot{\psi}_{rev}^{tr} = \sum_{\alpha=1}^{24} X^{\alpha} \dot{\xi}_{rev}^{\alpha} \tag{13}$$

X^{α} represents the resistance to phase transformation.

It should be noted that the rated form of parameters ψ^{int} and ψ_{rev}^{tr} are presented since their changes are important not their values. In addition, parameters $\mathbf{B}$ and X^{α} are not constant and evolve during phase transformation.

As the internal stress is caused by martensite variants, it can be divided into 24 components [23]:

$$\mathbf{B} = \sum_{\alpha=1}^{24} \left\| \mathbf{B}^{\alpha} \right\| \mathbf{P}^{\alpha}, \qquad \left\| \mathbf{B}^{\alpha} \right\| = B_{sat}(1 - \exp(-b_6 \bar{\xi}_{rev}^{\alpha})) \tag{14}$$

where $\left\| \mathbf{B}^{\alpha} \right\|$ is the norm of $\mathbf{B}^{\alpha}$ (the internal stress caused by the α-th martensite variant). b_6 is the parameter which controls the saturation rate of $\left\| \mathbf{B}^{\alpha} \right\|$, B_{sat} is the saturation value of $\mathbf{B}^{\alpha}$. For simplicity, it is assumed that the internal stress is a function of accumulated reversible martensite volume fraction $\bar{\xi}_{rev}^{\alpha}$ [25], which is shown in the rate-form by:

$$\dot{\bar{\xi}}_{rev}^{\alpha} = \left| \dot{\xi}_{rev}^{\alpha} \right| \tag{15}$$

As transformation hardening occurs during cyclic deformation, $\mathbf{X}^{\alpha}$ is considered as a function of the reversible martensite volume fraction [23].

$$X^{\alpha} = H^{\alpha}_{rev}\xi^{\alpha}_{rev}, \qquad H^{\alpha}_{rev} = H_0 + (H_{sat} - H_0)(1 - \exp(-b_4\bar{\xi}^{\alpha}_{rev})) \tag{16}$$

where H^{α}_{rev} is a hardening modulus and a function of accumulated reversible martensite volume fraction $\bar{\xi}^{\alpha}_{rev}$. H_0 and H_{sat} are initial and saturation values of H^{α}_{rev}, respectively. The parameter b_4 controls the evolution rate of H^{α}_{rev} during cyclic loading.

Using the 2nd law of thermodynamics and the Helmholtz free energy, the Clausius dissipation inequality can be written as [18,19]:

$$-\eta\dot{\theta} - \dot{\psi} - \frac{1}{\theta}\mathbf{q}_0.\nabla\theta + \mathbf{S} : \dot{\mathbf{F}} \geq 0 \tag{17}$$

where $\mathbb{S}$ is the first Piola–Kirchhoff stress tensor. Considering quasi-static loading conditions, the temperature can be assumed homogeneous inside a crystal. Neglecting the transformation latent heat and the heat from internal dissipation, the third term in Eq. (17) can be neglected. Using the equality $\mathbf{S} : \dot{\mathbf{F}} = \mathbf{T}^* : \dot{\mathbf{E}}^e + (\mathbf{C}^e\mathbf{T}^*) : \mathbf{L}^P$, and considering quasi-static loading, Eq. (17) can be re-written as:

$$\mathbf{T}^* : \dot{\mathbf{E}}^e + (\mathbf{C}^e\mathbf{T}^*) : \mathbf{L}^P - \eta\dot{\theta} - \dot{\psi} \geq 0 \tag{18}$$

where $\mathbf{T}^* = (\det\mathbf{F})\mathbf{F}^{e^{-1}}\mathbf{T}\mathbf{F}^{e^{-T}}$ is the second Piola–Kirchhoff stress tensor associated with the elastic part, and $\mathbb{T}$ is the Cauchy stress tensor.

Using Eqs. (10) and (11), $\dot{\psi}^e$ and $\dot{\psi}^{ch}$ are expressed by:

$$\dot{\psi}^e = \frac{\partial\psi^e}{\partial\mathbf{E}^e} : \dot{\mathbf{E}}^e + \frac{\partial\psi^e}{\partial\xi}\dot{\xi} \tag{19.a}$$

$$\dot{\psi}^{ch} = \frac{\partial\psi^{ch}}{\partial\theta}\dot{\theta} + \frac{\partial\psi^{ch}}{\partial\xi}\dot{\xi} \tag{19.b}$$

where:

$$\frac{\partial\psi^e}{\partial\mathbf{E}^e} = \mathbb{C}\mathbf{E}^e, \qquad \frac{\partial\psi^e}{\partial\xi} = \frac{1}{2}\mathbf{E}^e.(\Delta\mathbb{C}\mathbf{E}^e), \qquad \Delta\mathbb{C} = \mathbb{C}_M - \mathbb{C}_A \tag{20.a}$$

$$\frac{\partial\psi^{ch}}{\partial\theta} = \frac{h_T}{\theta_T}\xi, \qquad \frac{\partial\psi^{ch}}{\partial\xi} = \frac{h_T}{\theta_T}(\theta - \theta_T) \tag{20.b}$$

Using Eqs. (12), (13), and (19), Eq. (18) can be re-written as:

$$\mathbf{T}^{*}:\dot{\mathbf{E}}^{e}+(\mathbf{C}^{e}\mathbf{T}^{*}):\mathbf{L}^{P}-\eta\dot{\theta}-\frac{\partial\psi^{e}}{\partial\mathbf{E}^{e}}:\dot{\mathbf{E}}^{e}-\frac{\partial\psi^{e}}{\partial\xi}\dot{\xi}$$
$$-\frac{\partial\psi^{ch}}{\partial\theta}\dot{\theta}-\frac{\partial\psi^{ch}}{\partial\xi}\dot{\xi}+\mathbf{B}:\mathbf{L}^{P}-\sum_{\alpha=1}^{24}X^{\alpha}\dot{\xi}_{rev}^{\alpha}\geq 0 \tag{21}$$

Considering the special case when $\dot{\xi}_{rev}^{\alpha}=\dot{\xi}_{ire}^{\alpha}=\dot{\gamma}_{TRIP}^{\alpha}=\dot{\lambda}^{\alpha}=\dot{\gamma}_{DIP}^{\alpha}=0$, since either positive or negative values can be assigned to the parameters $\dot{\mathbf{E}}^{e}$ and $\dot{\theta}$, the necessary condition for Eq. (21) to be satisfied is that:

$$\mathbf{T}^{*}=\frac{\partial\psi^{e}}{\partial\mathbf{E}^{e}}=\mathbb{C}\mathbf{E}^{e} \tag{22}$$

$$\eta=-\frac{\partial\psi^{ch}}{\partial\theta}=-\frac{h_{T}}{\theta_{T}}\xi \tag{23}$$

Using Eqs. (21-23), the dissipation inequality can be stated by:

$$(\mathbf{C}^{e}\mathbf{T}^{*}+\mathbf{B}):(\sum_{\alpha=1}^{24}\dot{\xi}_{rev}^{\alpha}g^{tr}\mathbf{P}^{\alpha}+\sum_{\alpha=1}^{24}\dot{\xi}_{ire}^{\alpha}g^{tr}\mathbf{P}^{\alpha}+\sum_{\alpha=1}^{24}\dot{\gamma}_{TRIP}^{\alpha}\mathbf{P}^{\alpha}+\sum_{\alpha=1}^{24}\dot{\lambda}^{\alpha}\xi^{\alpha}\mathbf{P}_{\det}^{\alpha}+\sum_{\alpha=1}^{24}\dot{\gamma}_{DIP}^{\alpha}\mathbf{P}_{\det}^{\alpha})$$
$$-\sum_{\alpha=1}^{24}\frac{\partial\psi^{e}}{\partial\xi_{rev}^{\alpha}}\dot{\xi}_{rev}^{\alpha}-\sum_{\alpha=1}^{24}\frac{\partial\psi^{e}}{\partial\xi_{ire}^{\alpha}}\dot{\xi}_{ire}^{\alpha}-\sum_{\alpha=1}^{24}\frac{\partial\psi^{ch}}{\partial\xi_{rev}^{\alpha}}\dot{\xi}_{rev}^{\alpha}-\sum_{\alpha=1}^{24}\frac{\partial\psi^{ch}}{\partial\xi_{ire}^{\alpha}}\dot{\xi}_{ire}^{\alpha}-\sum_{\alpha=1}^{24}X^{\alpha}\dot{\xi}_{rev}^{\alpha}\geq 0 \tag{24}$$

Since different processes of reversible phase transformation, irreversible phase transformation, detwinning, transformation-induced plasticity, and detwinning-induced plasticity, are all energy dissipative processes, according to the stronger form of Eq. (24), the energy dissipation of each part can be considered to be non-negative.

$$\sum_{\alpha=1}^{24}((\mathbf{C}^{e}\mathbf{T}^{*}+\mathbf{B}):g^{tr}\mathbf{P}^{\alpha}-\frac{\partial\psi^{e}}{\partial\xi_{rev}}-\frac{\partial\psi^{ch}}{\partial\xi_{rev}}-X^{\alpha})\dot{\xi}_{rev}^{\alpha}\geq 0 \tag{25.a}$$

$$\sum_{\alpha=1}^{24}((\mathbf{C}^{e}\mathbf{T}^{*}+\mathbf{B}):g^{tr}\mathbf{P}^{\alpha}-\frac{\partial\psi^{e}}{\partial\xi_{ire}}-\frac{\partial\psi^{ch}}{\partial\xi_{ire}})\dot{\xi}_{ire}^{\alpha}\geq 0 \tag{25.b}$$

$$\sum_{\alpha=1}^{24}((\mathbf{C}^{e}\mathbf{T}^{*}+\mathbf{B}):\mathbf{P}^{\alpha})\dot{\gamma}_{TRIP}^{\alpha}\geq 0 \tag{25.c}$$

$$\sum_{\alpha=1}^{24}((\mathbf{C}^{e}\mathbf{T}^{*}+\mathbf{B}):\mathbf{P}_{\det}^{\alpha}\xi^{\alpha})\dot{\lambda}^{\alpha}\geq 0 \tag{25.d}$$

$$\sum_{\alpha=1}^{24}((\mathbf{C}^{e}\mathbf{T}^{*}+\mathbf{B}):\mathbf{P}_{\det}^{\alpha})\dot{\gamma}_{DIP}^{\alpha}\geq 0 \tag{25.e}$$

It is assumed that the dissipation inequality is non-negative for all variants. Therefore, each dissipation part in Eq. (25) can be divided into 24 components, i.e.,

$$((\mathbf{C}^e\mathbf{T}^* + \mathbf{B}) : g^{tr}\mathbf{P}^\alpha - \frac{\partial \psi^e}{\partial \xi_{rev}} - \frac{\partial \psi^{ch}}{\partial \xi_{rev}} - X^\alpha)\dot{\xi}^\alpha_{rev} \geq 0 \qquad \alpha=1,2,...,24 \tag{26.a}$$

$$((\mathbf{C}^e\mathbf{T}^* + \mathbf{B}) : g^{tr}\mathbf{P}^\alpha - \frac{\partial \psi^e}{\partial \xi_{ire}} - \frac{\partial \psi^{ch}}{\partial \xi_{ire}})\dot{\xi}^\alpha_{ire} \geq 0 \qquad \alpha=1,2,...,24 \tag{26.b}$$

$$((\mathbf{C}^e\mathbf{T}^* + \mathbf{B}) : \mathbf{P}^\alpha)\dot{\gamma}^\alpha_{TRIP} \geq 0 \qquad \alpha=1,2,...,24 \tag{26.c}$$

$$((\mathbf{C}^e\mathbf{T}^* + \mathbf{B}) : \mathbf{P}^\alpha_{\det}\xi^\alpha)\dot{\lambda}^\alpha \geq 0 \qquad \alpha=1,2,...,24 \tag{26.d}$$

$$((\mathbf{C}^e\mathbf{T}^* + \mathbf{B}) : \mathbf{P}^\alpha_{\det})\dot{\gamma}^\alpha_{DIP} \geq 0 \qquad \alpha=1,2,...,24 \tag{26.e}$$

Therefore, the dissipation inequalities, in terms of the thermodynamics driving forces and their conjugate variables, are expressed as follows:

$$\pi^\alpha_{rev}\dot{\xi}^\alpha_{rev} \geq 0 \qquad \alpha=1,2,...,24 \tag{27.a}$$

$$\pi^\alpha_{ire}\dot{\xi}^\alpha_{ire} \geq 0 \qquad \alpha=1,2,...,24 \tag{27.b}$$

$$\pi^\alpha_{TRIP}\dot{\gamma}^\alpha_{TRIP} \geq 0 \qquad \alpha=1,2,...,24 \tag{27.c}$$

$$\pi^\alpha_{\det}\dot{\lambda}^\alpha \geq 0 \qquad \alpha=1,2,...,24 \tag{27.d}$$

$$\pi^\alpha_{DIP}\dot{\gamma}^\alpha_{DIP} \geq 0 \qquad \alpha=1,2,...,24 \tag{27.e}$$

where π^α_{rev}, π^α_{ire}, π^α_{TRIP}, $\pi^\alpha_{\det}$, and π^α_{DIP} are the thermodynamic driving forces related to reversible phase transformation, irreversible phase transformation (residual martensite), transformation-induced plasticity, detwinning, and detwinning-induced plasticity, respectively.

$$\pi^\alpha_{rev} = (\mathbf{C}^e\mathbf{T}^* + \mathbf{B}) : g^{tr}\mathbf{P}^\alpha - \frac{\partial \psi^e}{\partial \xi_{rev}} - \frac{\partial \psi^{ch}}{\partial \xi_{rev}} - X^\alpha \tag{28.a}$$

$$\pi^\alpha_{ire} = (\mathbf{C}^e\mathbf{T}^* + \mathbf{B}) : g^{tr}\mathbf{P}^\alpha - \frac{\partial \psi^e}{\partial \xi_{ire}} - \frac{\partial \psi^{ch}}{\partial \xi_{ire}} \tag{28.b}$$

$$\pi^\alpha_{TRIP} = (\mathbf{C}^e\mathbf{T}^* + \mathbf{B}) : \mathbf{P}^\alpha \tag{28.c}$$

$$\pi^\alpha_{\det} = (\mathbf{C}^e\mathbf{T}^* + \mathbf{B}) : \mathbf{P}^\alpha_{\det}\xi^\alpha \tag{28.d}$$

$$\pi^\alpha_{DIP} = (\mathbf{C}^e\mathbf{T}^* + \mathbf{B}) : \mathbf{P}^\alpha_{\det} \tag{28.e}$$

2.2.Evolution equations for internal variables

2.2.1. Evolution equations for reversible phase transformation

According to Eq. (27.a), π_{rev}^{α} and $\dot{\xi}_{rev}^{\alpha}$ should always have the same sign. $\dot{\xi}_{rev}^{\alpha}$ captures positive values during forward, and negative values during reverse transformation. Therefore, in order to satisfy the 2nd law of thermodynamics, π_{rev}^{α} should be non-negative during forward, and non-positive during reverse transformation. In the case of elastic loading/unloading, there is no phase transformation, $\dot{\xi}_{rev}^{\alpha}$ is equal to zero, and entropy inequality is automatically satisfied. Adopting the concept of transformation functions [30,37], the evolution equations for the reversible martensite volume fraction are as follows:

$$\dot{\xi}_{rev}^{\alpha} = \begin{cases} \left| \dfrac{\pi_{rev}^{\alpha}}{Y} \right|^{n_{tr}} & \text{if} \quad \pi_{rev}^{\alpha} > 0, \quad \xi^{\alpha} < 1, \quad \xi < 1 \\ -\left| \dfrac{\pi_{rev}^{\alpha}}{b_5 Y} \right|^{n_{tr}} & \text{if} \quad \pi_{rev}^{\alpha} < 0, \quad \xi^{\alpha} > \xi_{ire}^{\alpha}, \quad \xi > \xi_{ire} \\ 0 & \text{other conditions} \end{cases} \tag{29}$$

where Y is the resistance to phase transformation. b_5 reflects the difference in evolution of reversible martensite volume fraction during forward and reverse transformations. The rate sensitivity of martensite transformation is controlled by n_{tr}. The parameter Y controls the width of hysteresis loop, and is dependent on martensite volume fraction:

$$Y = Y_0 + Y_d \xi_{rev} \tag{30}$$

where Y_0 is the initial value of Y, and Y_d describes the dependence of Y on the reversible martensite volume fraction.

2.2.2. Evolution equations for transformation-induced plasticity

Since transformation-induced plasticity is an irreversible dissipation process, $\dot{\gamma}_{TRIP}^{\alpha}$ is always non-negative, i.e., $\dot{\gamma}_{TRIP}^{\alpha} \geq 0$. Considering Eq. (27.c), the constraint for TRIP can be described as:

$$\begin{cases} \dot{\gamma}_{TRIP}^{\alpha} > 0 & \pi_{TRIP}^{\alpha} \geq 0 \quad (31.a) \\ \dot{\gamma}_{TRIP}^{\alpha} = 0 & \text{no constraint} \quad (31.b) \end{cases}$$

Using Eq. (31), an evolution equation for TRIP can be expressed as [23]:

$$\dot{\gamma}^{\alpha}_{TRIP} = b_2 \left\langle \gamma^{sat}_{TRIP} - \gamma^{\alpha}_{TRIP} \right\rangle \left| \dot{\xi}^{\alpha} \right| H(\pi^{\alpha}_{TRIP}) \tag{32}$$

where $\langle x \rangle$ and $H(x)$ are McCauley bracket and step function, respectively. b_2 controls the saturation rate of γ^{α}_{TRIP}, and γ^{sat}_{TRIP} is the saturated value of γ^{α}_{TRIP}. $H\left(\pi^{\alpha}_{TRIP}\right)$ guarantees that $\dot{\gamma}^{\alpha}_{TRIP}$ is always positive and the 2nd law of thermodynamics is satisfied.

2.2.3. Evolution equations for irreversible phase transformation

Since the formation of residual martensite is an irreversible dissipative process, the condition for irreversible martensite volume fraction to satisfy the 2nd law of thermodynamics is:

$$\begin{cases} \dot{\xi}^{\alpha}_{ire} > 0 & \pi^{\alpha}_{ire} \geq 0 \quad (33.a) \\ \dot{\xi}^{\alpha}_{ire} = 0 & \text{no constraint} \quad (33.b) \end{cases}$$

The amount of residual martensite increases with increasing number of cycles, eventually reaching a saturated value. As commented by Liu et al. [31], under tensile loading a flat stress-plateau is observed in the stress-strain response of the material, while under compression no plateau is seen and a high rate of strain hardening occurs. Higher material hardening under compression compared to tension is related to generation and migration of dislocations [31]. Additionally, accumulation of residual martensite is related to that part of martensite variants which is locked by increase of defects and cannot transform back to austenite [23]. Therefore, it is concluded that the amount of residual martensite should be higher in compression than in tension, which is also supported by the experimental results of Thamburaja and Anand [15]. In order to reflect the difference of residual martensite volume fraction in tension and compression, separate saturation values of this parameter are assigned for tension and compression. Therefore the evolution equation for residual martensite volume fraction is proposed here as:

$$\dot{\xi}^{\alpha}_{irev} = \begin{cases} \left\langle \xi^{sat}_{irev} - \xi^{\alpha}_{irev} \right\rangle \left| \dot{\xi}^{\alpha}_{rev} \right| H(\pi^{\alpha}_{irev}) & \text{for tension} \\ \left\langle b_1 \xi^{sat}_{irev} - \xi^{\alpha}_{irev} \right\rangle \left| \dot{\xi}^{\alpha}_{rev} \right| H(\pi^{\alpha}_{irev}) & \text{for compression} \end{cases} \tag{34}$$

where ξ^{sat}_{irev} is the saturated value of ξ^{α}_{irev}, and b_1 controls the saturation value of ξ^{α}_{irev} in compressive loading.

2.2.4. Evolution equations for detwinning

Considering Eq. (27.d) and using a power-law form, an evolution equation for detwinning of the α-th martensite variant is expressed as:

$$\dot{\lambda}^{\alpha} = \left| \frac{\pi_{\mathrm{det}}^{\alpha}}{K_{\mathrm{det}}} \right|^{n_{\mathrm{det}}} sign(\pi_{\mathrm{det}}^{\alpha}) \tag{35}$$

Since $\dot{\lambda}^{\alpha}$ can assume negative, zero, or positive values, $sign(\pi_{\mathrm{det}}^{\alpha})$ ensures that the second law of thermodynamics is always satisfied. K_{det} represents resistance to detwinning. n_{det} is a parameter used to determine the degree of dependence of the process on the loading rate and the higher its value, the lower the dependence of the detwinning process on the loading rate. It should be noted that, depending on the sign of $\pi_{\mathrm{det}}^{\alpha}$, the volume fraction of sub-variants can decrease or increase during loading.

2.2.5. Evolution equations for detwinning-induced plasticity

Since DIP is an irreversible dissipative process, $\dot{\gamma}_{DIP}^{\alpha}$ will always be non-negative, i.e., $\dot{\gamma}_{DIP}^{\alpha} \geq 0$. Therefore, the condition for $\dot{\gamma}_{DIP}^{\alpha}$ to satisfy the 2nd law of thermodynamics is:

$$\begin{cases} \dot{\gamma}_{DIP}^{\alpha} > 0 & \text{if } \pi_{DIP}^{\alpha} \geq 0 \quad (36.a) \\ \dot{\gamma}_{DIP}^{\alpha} = 0 & \text{no constraint} \quad (36.b) \end{cases}$$

According to the experimental observations [38], the residual and peak strains accumulate during cyclic loading of NiTi and will be saturated after some cycles. Using this fact and Eqs. (27.e), (36.a), and (36.b), the evolution equation for $\dot{\gamma}_{DIP}^{\alpha}$ is such that [32]:

$$\dot{\gamma}_{DIP}^{\alpha} = b_3 \left\langle \gamma_{DIP}^{sat} - \gamma_{DIP}^{\alpha} \right\rangle \left| \dot{\xi}^{\alpha} \right| H(\pi_{DIP}^{\alpha}) \tag{37}$$

where b_3 is a parameter controlling the saturation rate of detwinning-induced plasticity, γ_{DIP}^{sat} is the saturation value of γ_{DIP}. $H\left(\pi_{DIP}^{\alpha}\right)$ is used to ensure that Eq. (27.e) is always satisfied, so that , $\dot{\gamma}_{DIP}^{\alpha} > 0$ if $\pi_{DIP}^{\alpha} > 0$, and $\dot{\gamma}_{DIP}^{\alpha} = 0$ if $\pi_{DIP}^{\alpha} \leq 0$. A summary of the proposed constitutive model at the single-crystal scale is presented in Table 1.

Table 1: Summary of the proposed constitutive model

$\mathbf{F} = \mathbf{F}^e\mathbf{F}^p$	Deformation gradient tensor
$\mathbf{L}^{tr} = \mathbf{L}^{tr}_{rev} + \mathbf{L}^{tr}_{ire} = \sum_{\alpha=1}^{24} \dot{\xi}^{\alpha}_{rev} g^{tr}\mathbf{P}^{\alpha} + \sum_{\alpha=1}^{24} \dot{\xi}^{\alpha}_{ire} g^{tr}\mathbf{P}^{\alpha}$	Velocity gradient tensor
$\mathbf{L}^{TRIP} = \sum_{\alpha=1}^{24} \dot{\gamma}^{\alpha}_{TRIP}\mathbf{P}^{\alpha}$	
$\mathbf{L}^{\det} = \sum_{\alpha=1}^{24} \dot{\lambda}^{\alpha}\xi^{\alpha}\mathbf{P}^{\alpha}_{\det},$	
$\mathbf{L}^{DIP} = \sum_{\alpha=1}^{24} \dot{\gamma}^{\alpha}_{DIP}\mathbf{P}^{\alpha}_{\det}$	
$\pi^{\alpha}_{rev} = (\mathbf{C}^e\mathbf{T}^* + \mathbf{B}) : g^{tr}\mathbf{P}^{\alpha} - \frac{\partial\psi^e}{\partial\xi_{rev}} - \frac{\partial\psi^{ch}}{\partial\xi_{rev}} - X^{\alpha}$	Thermodynamic deriving forces
$\pi^{\alpha}_{ire} = (\mathbf{C}^e\mathbf{T}^* + \mathbf{B}) : g^{tr}\mathbf{P}^{\alpha} - \frac{\partial\psi^e}{\partial\xi_{ire}} - \frac{\partial\psi^{ch}}{\partial\xi_{ire}}$	
$\pi^{\alpha}_{TRIP} = (\mathbf{C}^e\mathbf{T}^* + \mathbf{B}) : \mathbf{P}^{\alpha}$	
$\pi^{\alpha}_{\det} = (\mathbf{C}^e\mathbf{T}^* + \mathbf{B}) : \mathbf{P}^{\alpha}_{\det}\xi^{\alpha}$	
$\pi^{\alpha}_{DIP} = (\mathbf{C}^e\mathbf{T}^* + \mathbf{B}) : \mathbf{P}^{\alpha}_{\det}$	
$\dot{\xi}^{\alpha}_{rev} = \begin{cases} \left\lvert\frac{\pi^{\alpha}_{rev}}{Y}\right\rvert^{n_{tr}} & \text{if } \pi^{\alpha}_{rev} > 0, \quad \xi^{\alpha} < 1, \quad \xi < 1 \\ -\left\lvert\frac{\pi^{\alpha}_{rev}}{b_5 Y}\right\rvert^{n_{tr}} & \text{if } \pi^{\alpha}_{rev} < 0, \quad \xi^{\alpha} > \xi^{\alpha}_{ire}, \quad \xi > \xi_{ire} \\ 0 & \text{other conditions} \end{cases}$	Evolution equations for reversible phase transformation
$\dot{\xi}^{\alpha}_{irev} = \begin{cases} \left\langle \xi^{sat}_{irev} - \xi^{\alpha}_{irev} \right\rangle \left\lvert \dot{\xi}^{\alpha}_{rev} \right\rvert H(\pi^{\alpha}_{irev}) & \text{for tension} \\ \left\langle b_1\xi^{sat}_{irev} - \xi^{\alpha}_{irev} \right\rangle \left\lvert \dot{\xi}^{\alpha}_{rev} \right\rvert H(\pi^{\alpha}_{irev}) & \text{for compression} \end{cases}$	Evolution equations for residual martensite
$\dot{\gamma}^{\alpha}_{TRIP} = b_2 \left\langle \gamma^{sat}_{TRIP} - \gamma^{\alpha}_{TRIP} \right\rangle \left\lvert \dot{\xi}^{\alpha} \right\rvert H(\pi^{\alpha}_{TRIP})$	Evolution equation for transformation-induced plasticity
$\dot{\lambda}^{\alpha} = \left\lvert\frac{\pi^{\alpha}_{\det}}{K_{\det}}\right\rvert^{n_{\det}} sign(\pi^{\alpha}_{\det})$	Evolution equation for detwinning
$\dot{\gamma}^{\alpha}_{DIP} = b_3 \left\langle \gamma^{sat}_{DIP} - \gamma^{\alpha}_{DIP} \right\rangle \left\lvert \dot{\xi}^{\alpha} \right\rvert H(\pi^{\alpha}_{DIP})$	Evolution equation for detwinning-induced plasticity

2.3 Calculation of stress

In order to model the behavior of NiTi SMAs under large deformations, the constitutive model has been implemented in the Abaqus/Explicit finite-element program, using VUMAT subroutine. The following describes how stress is calculated using the relationships presented in Section 2.

Using Eqs. (3) and (8), the plastic deformation gradient tensor is calculated as follows:

$$(\mathbf{F}^P)_{n+1} = (I + \sum_{\alpha=1}^{24} \Delta\xi^\alpha g^{tr}\mathbf{P}^\alpha + \sum_{\alpha=1}^{24} \Delta\gamma_{TRIP}^\alpha \mathbf{P}^\alpha + \sum_{\alpha=1}^{24} \Delta\lambda^\alpha \xi^\alpha \mathbf{P}_{\det}^\alpha + \sum_{\alpha=1}^{24} \Delta\gamma_{DIP}^\alpha \mathbf{P}_{\det}^\alpha)(\mathbf{F}^P)_n \tag{38}$$

where $(\mathbf{F}^P)_{n+1}$ is the plastic deformation gradient tensor in the $(n+1)-\text{th}$ increment, and $(\mathbf{F}^P)_n$ is the corresponding variable in the $n-\text{th}$ increment. Using Eq. (1), With $\mathbf{F}$ and $\mathbf{F}^p$ to be known, the elastic deformation gradient tensor can be determined.

$$\mathbf{F}^e = \mathbf{F}\mathbf{F}^{p^{-1}} \tag{39}$$

The elastic Green-Lagrange strain tensor, in terms of the elastic deformation gradient tensor, is calculated such that [18]:

$$\mathbf{E}^e = \frac{1}{2}(\mathbf{F}^{e^T}\mathbf{F}^e - \mathbf{I}) \tag{40}$$

Using $\mathbf{E}^e$ and $\mathbf{T}^*$ (Eq. (22)), the Cauchy stress tensor can be calculated.

$$\mathbf{T} = \frac{1}{\det\mathbf{F}}\mathbf{F}^e\mathbf{T}^*\mathbf{F}^{e^T} \tag{41}$$

3. Material parameters identification

Since three independent elastic coefficients can be used for materials with a cubic crystal structure, the fourth-order elasticity tensor is considered such that [39]:

$$\mathbb{C} = \begin{pmatrix} \mathbb{C}_{11} & \mathbb{C}_{12} & \mathbb{C}_{12} & 0 & 0 & 0 \\ \mathbb{C}_{12} & \mathbb{C}_{11} & \mathbb{C}_{12} & 0 & 0 & 0 \\ \mathbb{C}_{12} & \mathbb{C}_{12} & \mathbb{C}_{11} & 0 & 0 & 0 \\ 0 & 0 & 0 & \mathbb{C}_{44} & 0 & 0 \\ 0 & 0 & 0 & 0 & \mathbb{C}_{44} & 0 \\ 0 & 0 & 0 & 0 & 0 & \mathbb{C}_{44} \end{pmatrix} \tag{42}$$

The corresponding independent elastic constants for austenite phase are denoted by $\mathbb{C}_{11}^{A}$, $\mathbb{C}_{12}^{A}$, and $\mathbb{C}_{44}^{A}$, and considered to be 130, 98, and 34 GPa, respectively [15,40]. The elastic modulus of austenite is usually two to three times greater than the elastic modulus of martensite, and the Poisson's ratios for these two phases are almost the same. Therefore, the elastic constants of martensite ($\mathbb{C}_{11}^{M}, \mathbb{C}_{12}^{M}, \mathbb{C}_{44}^{M}$) are considered equal to half of the elastic constants of austenite [15].

In order to obtain the rate-independent response of NiTi SMAs, sufficiently large values are assigned to the parameters n_{tr} and n_{det}.

The evolution law of reversible martensite volume fraction during forward and reverse transformations is described by the parameters Y and b_5. The width of hysteresis loop for the first and steady-state cycles is controlled by the parameters Y_0 and Y_d, respectively. The parameter $\mathrm{K}_{\mathrm{det}}$ can be obtained by fitting the curves related to start-stress of detwinning.

As experimentally observed [31] and computationally predicted [32], the effect of DIP is not obvious during tensile loading. Therefore, the parameters related to DIP cannot be obtained by using the data related to tensile loading of SMA. On the other hand, as commented by Kang et al. [29], TRIP affects both the accumulated peak strain and accumulated residual strain during uniaxial cyclic deformation, while the influence of residual martensite is mainly focused on the accumulated residual strain. Thus, the data of accumulated peak strain in tensile cyclic loading can be used to obtain the parameters b_2 and γ_{TRIP}^{sat}. Using the data related to the difference of peak and residual strains in tensile and compressive cyclic loadings, the parameters b_1 and ξ_{irev}^{sat} can be obtained. The parameters b_3 and γ_{DIP}^{sat}, which are related to DIP, can be calibrated by using the evolution curves of residual strain under compressive loading.

Using transformation modulus at the first and steady-state cycles, the parameters H_0 and H_{sat} can be calibrated, respectively. $\mathrm{B}_{\mathrm{sat}}$, which is used to demonstrate the reduction in the start-stress of martensite transformation during cyclic loading, can be calibrated by measuring the start-stress of martensite transformation in the first and steady-state cycles. In order to control the saturation rates of $\left\|\mathbf{B}^{\alpha}\right\|$ and H^{α}, parameters b_6 and b_4 are used, respectively. Therefore, the evolution curves of decreased start-stress of martensite transformation and hardening

modulus can be used to obtain the values of b_6 and b_4, respectively. The maximum transformation strain is controlled by the parameter g^{tr}. The parameter h_T controls the temperature dependence of the driving force. The phase equilibrium temperature can be calculated by $\theta_T \equiv \frac{1}{2}(\theta_{ms} + \theta_{as})$, where θ_{ms} and θ_{as} are martensite and austenite start temperatures at stress-free conditions, respectively [15].

It should be noted that the stress-strain curves of a single crystal are needed to obtain the above-mentioned parameters, which are related to a single crystal. In the lack of experimental data for single crystal, the polycrystalline experimental data is used to calibrate the parameters by a trial-and-error method.

The parameters adopted to predict the behavior of NiTi SMA, considering the effect of residual martensite, are listed in Table 2.

Table 2: Parameters used to predict Nitinol behavior in tensile and compressive loads considering the effect of residual martensite accumulation

Parameter	Value	Unit
$\mathbb{C}_{11}^A$, $\mathbb{C}_{12}^A$, $\mathbb{C}_{44}^A$	130, 98, 34	GPa
$\mathbb{C}_{11}^M$, $\mathbb{C}_{12}^M$, $\mathbb{C}_{44}^M$	65, 49, 17	GPa
Y_0, Y_d	10.2, 0	MPa
n_{tr}, $n_{\det}$	50	-
$K_{\det}$	15	MPa
B_{sat}	1	MPa
H_0, H_{sat}	80, 1	MPa
g^{tr}	0.19	-
$b_1, b_2, b_3, b_4, b_5, b_6$	2.5, 1, 1, 1, 1.5, 1	-

h_T	140	MPa
$\theta,\ \theta_T$	298, 256	K
$\xi_{irev}^{sat},\ \gamma_{TRIP}^{sat},\ \gamma_{DIP}^{sat}$	0.1, 0, 0	-

The parameters used to predict the cyclic behavior of NiTi, considering the effects of DIP and TRIP are presented in Tables 3 and 4, respectively.

Table 3: Parameters used to predict the cyclic behavior of NiTi by considering the effect of detwinning-induced plasticity

Parameter	Value	Unit
$\mathbb{C}_{11}^{A},\ \mathbb{C}_{12}^{A},\ \mathbb{C}_{44}^{A}$	130, 98, 34	GPa
$\mathbb{C}_{11}^{M},\ \mathbb{C}_{12}^{M},\ \mathbb{C}_{44}^{M}$	65, 49, 17	GPa
$Y_0,\ Y_d$	10.2, 10	MPa
$n_{tr},\ n_{\det}$	50	-
$K_{\det}$	15	MPa
B_{sat}	50	MPa
$H_0,\ H_{sat}$	600, 0	MPa
g^{tr}	0.1708	-
b_1, b_2, b_3, b_4, b_6	1	-
h_T	100	MPa
$\theta,\ \theta_T$	298, 256	K
$\xi_{irev}^{sat},\ \gamma_{TRIP}^{sat},\ \gamma_{DIP}^{sat}$	0, 0, 0,001	-

Table 4: Parameters used to predict the behavior of NiTi SMA by considering the effect of transformation-induced plasticity

Parameter	Value	Unit
$\mathbb{C}_{11}^{A}$, $\mathbb{C}_{12}^{A}$, $\mathbb{C}_{44}^{A}$	130, 98, 34	GPa
$\mathbb{C}_{11}^{M}$, $\mathbb{C}_{12}^{M}$, $\mathbb{C}_{44}^{M}$	65, 49, 17	GPa
Y_0, Y_d	10.2, 10	MPa
n_{tr}, n_{det}	50	-
K_{det}	15	MPa
B_{sat}	50	MPa
H_0, H_{sat}	200, 800	MPa
g^{tr}	0.1708	-
$b_1, b_2, b_3, b_4, b_5, b_6$	1	-
h_T	100	MPa
θ, θ_T	298, 256	K
ξ_{irev}^{sat}, γ_{TRIP}^{sat}, γ_{DIP}^{sat}	0, 0.001, 0	-

4. Results and discussion

In polycrystalline shape memory alloys, manufacturing process can affect the crystallographic texture which is the main reason for tension-compression asymmetry observed in such materials [15]. As commented by Gall et al. [41], based on the method used to form an alloy, three different textures with different effects on the overall response can be formed: a $[100]$ texture making the mechanical response stiffer in tension than in compression, a $[111]$ texture causing softer response in tension than in compression, and a $[110]$ texture which almost has no effect on the mechanical responses in tension or compression.

It should be noted that the parameters related to phase transformation direction, normal to the phase transformation plane, and detwinning are expressed in a crystal local coordinate system. Therefore, a transformation of the deformation gradient tensor from poly-crystal to single-crystal coordinate system is performed at the beginning of each increment. At the end of calculations, the calculated stress tensor should be transformed back to poly-crystal coordinate system, which is done by using the rotation matrix Q.

Appropriate ranges of Euler angles have been calculated in order to model different textures. To this end, the single-crystal and poly-crystal coordinates are considered as local and global coordinate systems, respectively. According to the Bunge system, the orientation of each crystal can be identified using 3 Euler angles, φ, ψ, and θ. In this system, the rotation matrix in 3D is expressed as [42]:

$$Q(\varphi,\psi,\theta)=\begin{bmatrix} \cos\varphi\cos\theta-\sin\varphi\sin\theta\cos\psi & \sin\varphi\cos\theta+\cos\varphi\sin\theta\cos\psi & \sin\theta\sin\psi \\ -\cos\varphi\sin\theta-\sin\varphi\cos\theta\cos\psi & -\sin\varphi\sin\theta+\cos\varphi\cos\theta\cos\psi & \cos\theta\sin\psi \\ \sin\varphi\sin\psi & -\cos\varphi\sin\psi & \cos\psi \end{bmatrix} \tag{43}$$

In order to model crystals with [111] texture, the [111] direction of each crystal should be nearly parallel to the loading direction. A set of randomly generated Euler angles without any preferred orientation, is used to simulate a random texture/untextured polycrystalline material.

Using the proposed model, the behavior of a single-crystal for different textures under tensile and compressive strain-controlled loading-unloading is presented in Fig. 1.

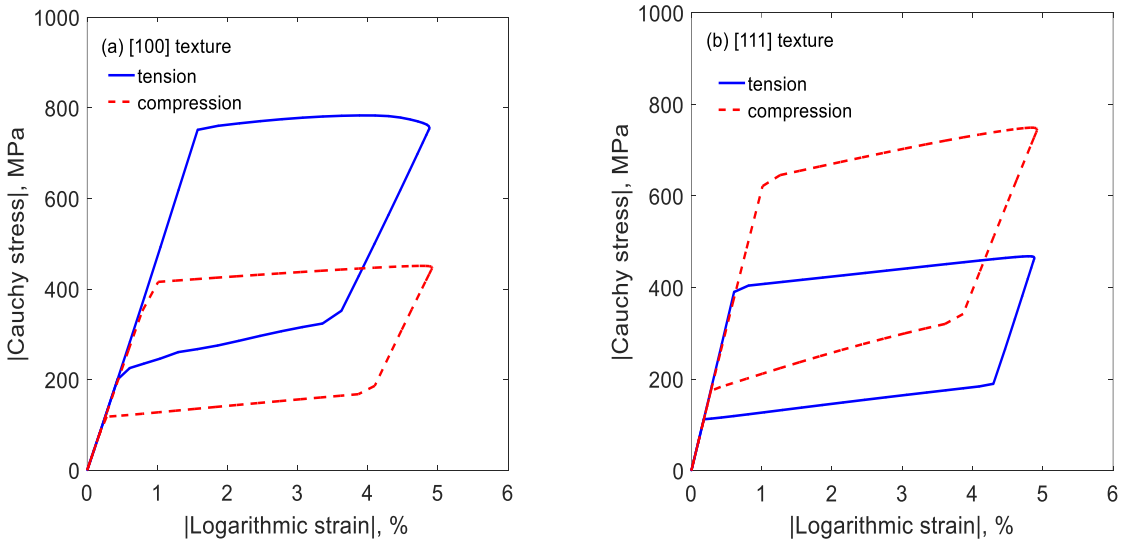

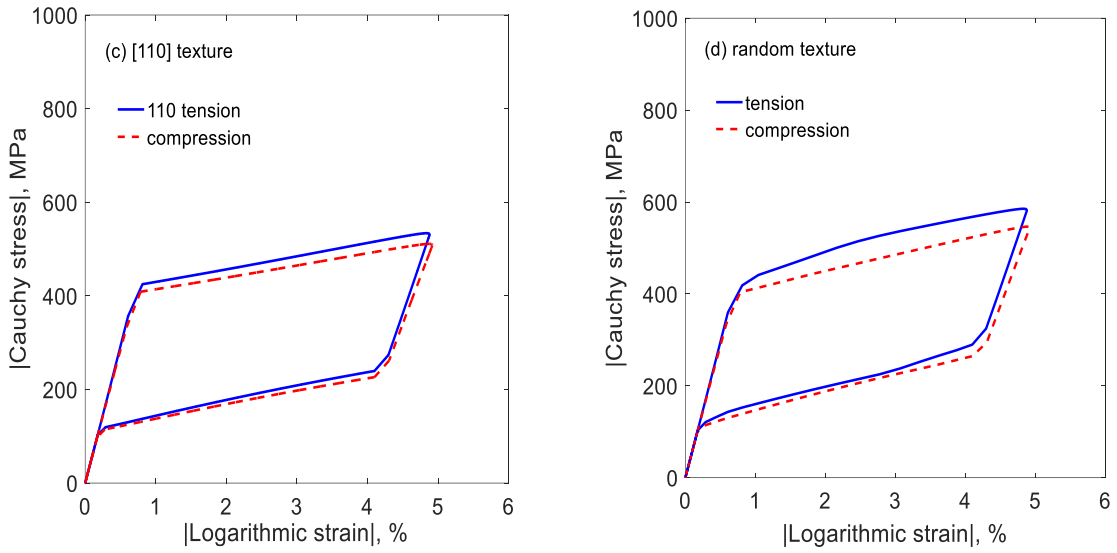

Fig. 1. Comparison of the behavior of NiTi SMA under tensile and compressive loads for different textures of crystals: (a) [100] texture, (b) [111] texture, (c) [110] texture, (d) Random texture. Magnitudes of Cauchy stress and logarithmic strain are presented for direct comparison of tension and compression.

As shown in Fig. 1, for [111] texture the material behavior is harder in compression than in tension. In contrast, for the two other textures, and also for the randomly oriented crystals, the behavior in compression is softer in compression than in tension. Tension-compression differences are less pronounced for [110] and random textures. Based on the asymmetrical tension/compression response observed in the experimental test of Thamburaja and Anand [15], the [111] texture is adopted to model the behavior of NiTi SMA in this work.

Since the number of crystals used to model the polycrystalline material can affect the predicted behavior, an appropriate number of crystals should be selected. The number of crystals should be as small as possible to reduce the computational cost and on the other hand should be large enough to prevent considerable change in material behavior by increasing number of crystals afterwards. Therefore, a sensitivity analysis is performed to determine the number of crystals in a representative volume element required for a converged stress-strain response. Results for 1, 8, 27, 64, and 125 crystals are shown in Fig. 2. Converged stress-strain behavior is obtained for 27, 64, and 125 crystals. Based on this sensitivity analysis 64 crystals will be used to model the polycrystalline behavior for the remainder of this study.

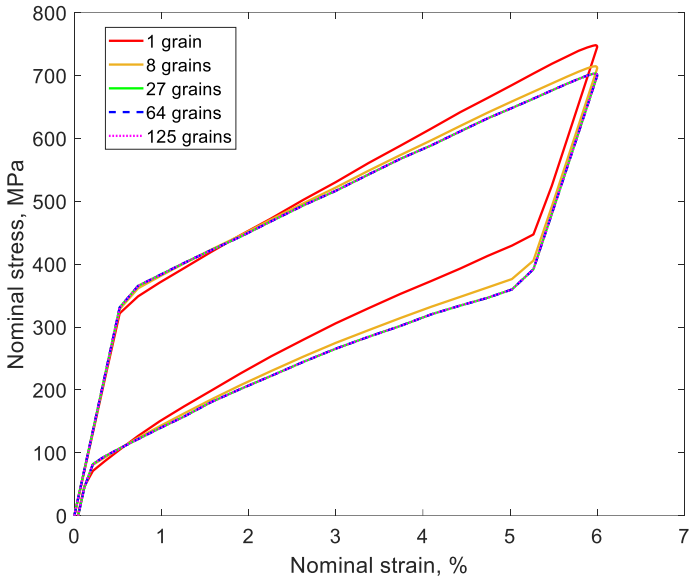

Fig. 2. Comparison of stress-strain curves of NiTi SMA for different number of crystals with a minimum strain of 0% and a maximum strain of 6%.

Von Mises stress distributions for 27, 64, and 125 crystals are shown in Fig. 3. Although different stress contours are obtained for different number of crystals, the stress-strain curves have the same trend in all three cases. Beside using various number of crystals, altering the randomly assigned orientations of the crystals changes the stress contours and locations of stress concentrations. However, the overall stress-strain response is independent of the randomly assigned orientations in all three cases. The Von Mises stress distributions for two various arrangements of crystals in a polycrystalline material with 125 crystals are presented in Fig. 4. It should be mentioned that the same sets of Euler angles have been used to capture [111] texture in both cases, but the Euler angles assigned to each crystal are randomly selected from that set in each case.

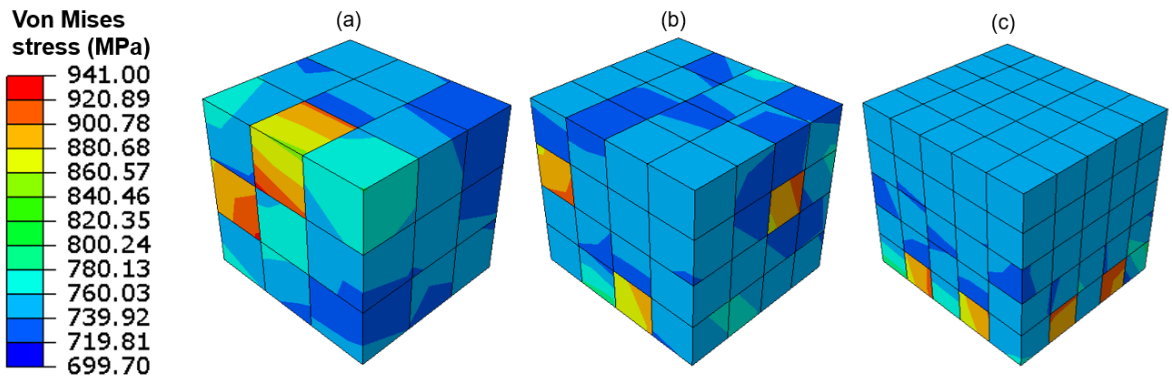

Fig. 3. Von Mises stress distribution at the end of loading for tension-unloading with a minimum strain of 0% and a maximum strain of 6% in a polycrystalline material with different number of crystals: (a) 27, (b) 64, and (c) 125 crystals.

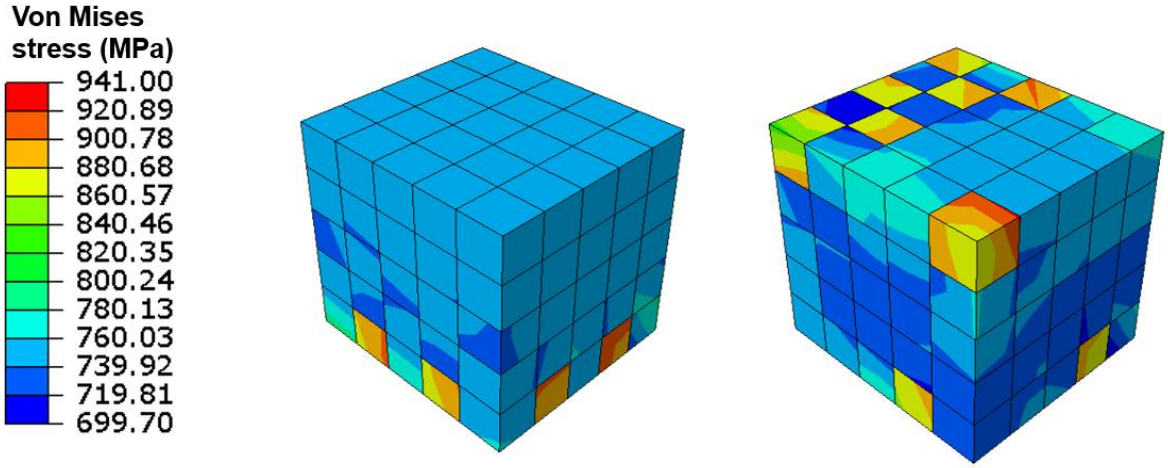

Fig. 4. Various Von Mises stress distributions for two different arrangements of crystals in a polycrystalline material with [111] texture composed of 125 crystals. The results are presented at the end of loading in tension-unloading with a minimum strain of 0% and a maximum strain of 6%).

In order to evaluate the proposed model, in Fig. 5 computed results for tensile and compressive loadings are directly compared with corresponding NiTi experimental data reported by Thamburaja and Anand [15]. The parameters used to model Nitinol's behavior are presented in Table 2. Several key features should be noted:

(i) the experimental results show residual strain after unloading, in both compression and tension. This is accurately predicted by the proposed model due to the incorporation of the effect of residual martensite. Experimental results of Liu et al. [31] show a stress-plateau in the stress-strain response during tensile loading, while the response is quickly strain hardened and no plateau is observed during compressive loading, which is related to the generation of

dislocations [31]. On the other hand, the increase of defects causes the residual martensite to be accumulated [23]. Using these 2 facts and the experimental results of Thamburaja and Anand [15], it is concluded that the amount of residual martensite should be higher in compression than in tension. In order to reflect the difference of residual martensite volume fraction in tension and compression, two separate values are assigned to the saturation value of this parameter for 2 loading cases in Eq. (34).

(ii) The proposed model accurately predicts the significant experimentally measured asymmetry between tension and compression, both in terms of loading and unloading behavior. As shown in Fig. 1, adopting [111] texture will cause to get a harder response in compression compared to tension. On the other hand, considering hardening/softening effects in the proposed model (Eq. (13)), the experimental results are predicted more precisely.

To highlight the improved predictions of the current model, corresponding predictions from the model of Thamburaja and Anand [15] are reproduced. This earlier model does not include the effects of residual martensite and hardening/softening effects during phase transformation, and therefore does not predict residual strain or increased hardening under compressive loading.

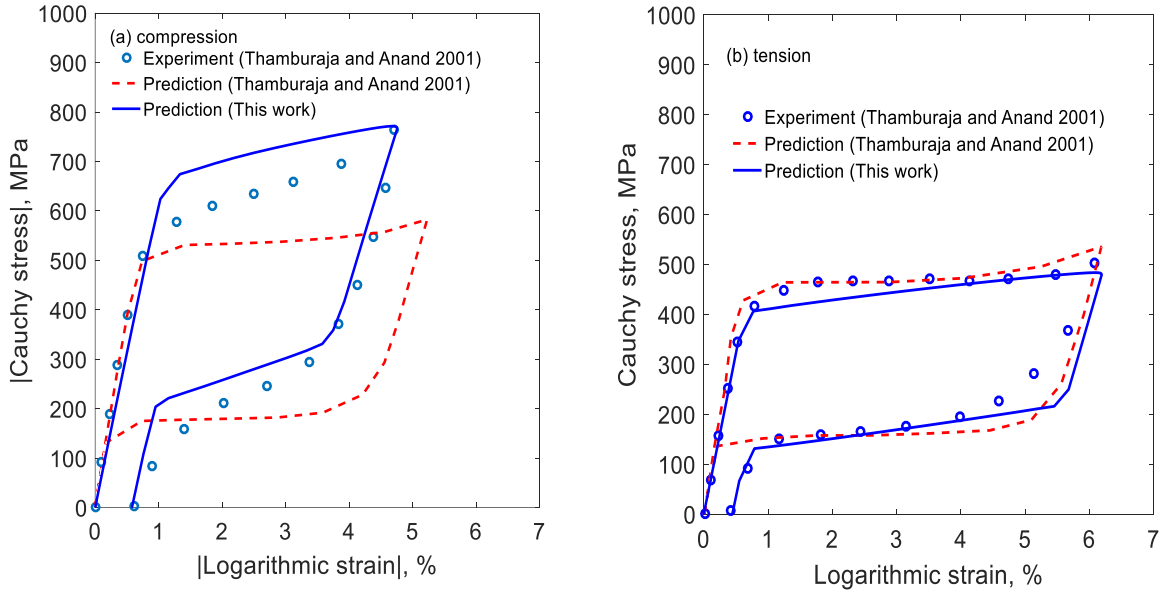

Fig. 5. Comparison of stress-strain curves of NiTi SMA with experimental results and available analytical results for two loading cases: (a) compression with a minimum strain of -5% and unloading to zero stress, (b) tension with a maximum strain of 6% and unloading to zero stress.

The distributions of Von Mises stresses and residual martensite volume fractions for the aforementioned compressive and tensile loading cases are shown in Figs. 6 and 7, respectively.

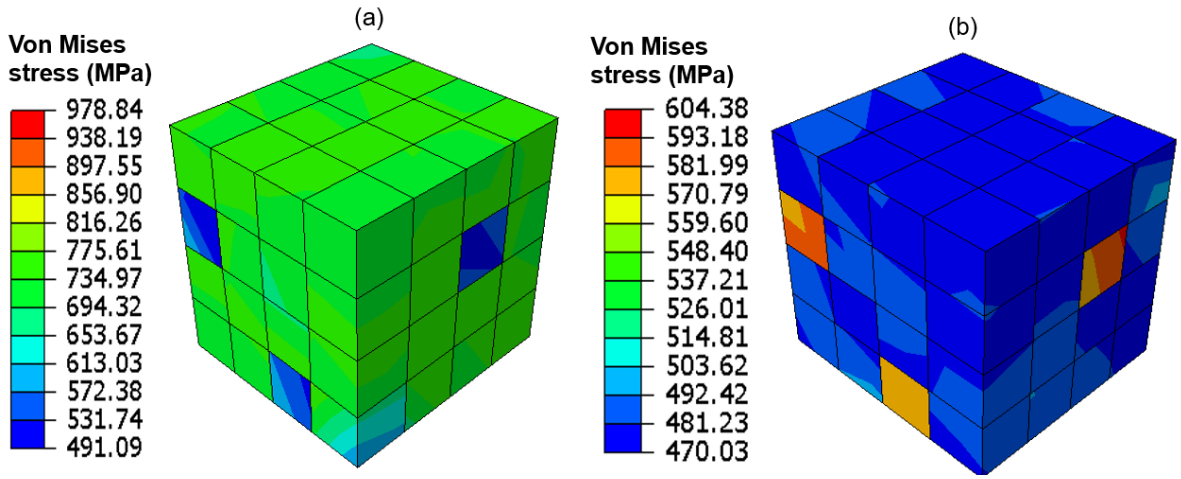

Fig. 6. Von Mises stress distributions at the end of loading for (a) compression-unloading with a minimum strain of -5% and unloading to zero stress, (b) tension-unloading with a maximum strain of 6% and unloading to zero stress.

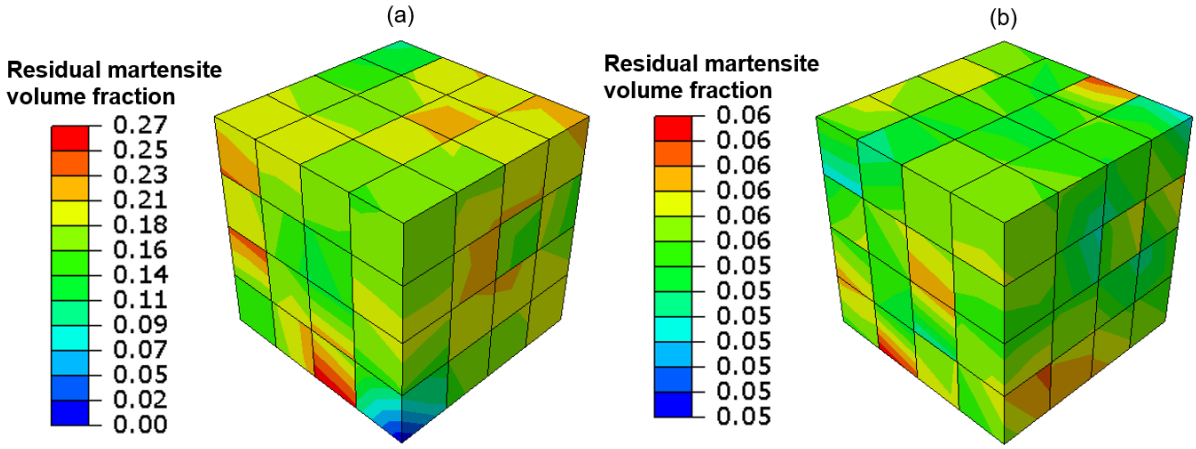

Fig. 7. Distribution of residual martensite volume fraction at the end of unloading for (a) compression-unloading with a minimum strain of -5% and unloading to zero stress, (b) tension-unloading with a maximum strain of 6% and unloading to zero stress.

The ability of the proposed model in predicting the cyclic behavior of NiTi SMA is shown in Fig. 8. The stress-strain curves are plotted for the first 5 cycles in tensile loading-unloading with a minimum stress of 0 MPa and a maximum stress of 550 MPa.

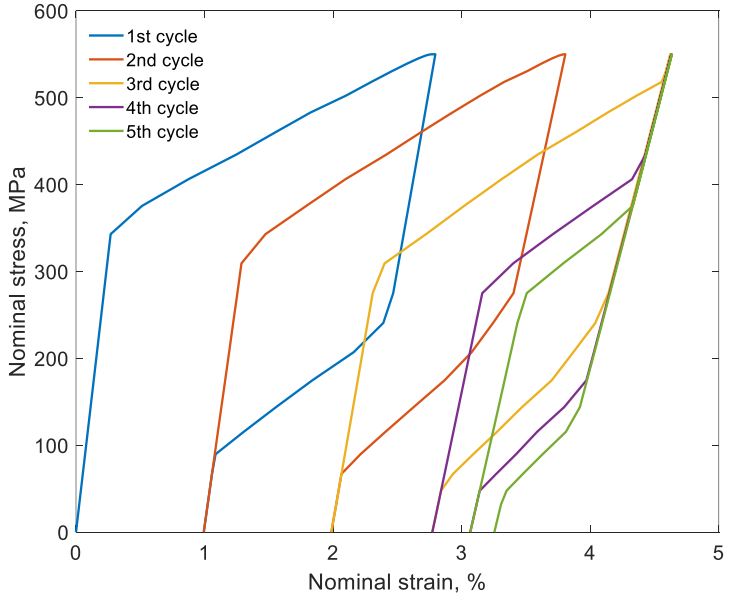

Fig. 8. NiTi SMA stress-strain diagrams under tensile loading-unloading with a minimum stress of 0 MPa and a maximum stress of 550 MPa.

The proposed model captures the main features observed in the experimental tests [29,38]. In summary, with increasing number of cycles, the start stress of austenite to martensite transformation decreases, the width of the hysteresis loop decreases, and the residual strain approaches a steady state, indicating that the accumulation of residual martensite approaches a saturation level.

In order to investigate the effect of DIP in large deformation, the stress-strain diagrams of the material under compressive loading to a minimum strain of -5% and unloading to zero stress are shown for the first, fifth and tenth cycles in Fig. 9.

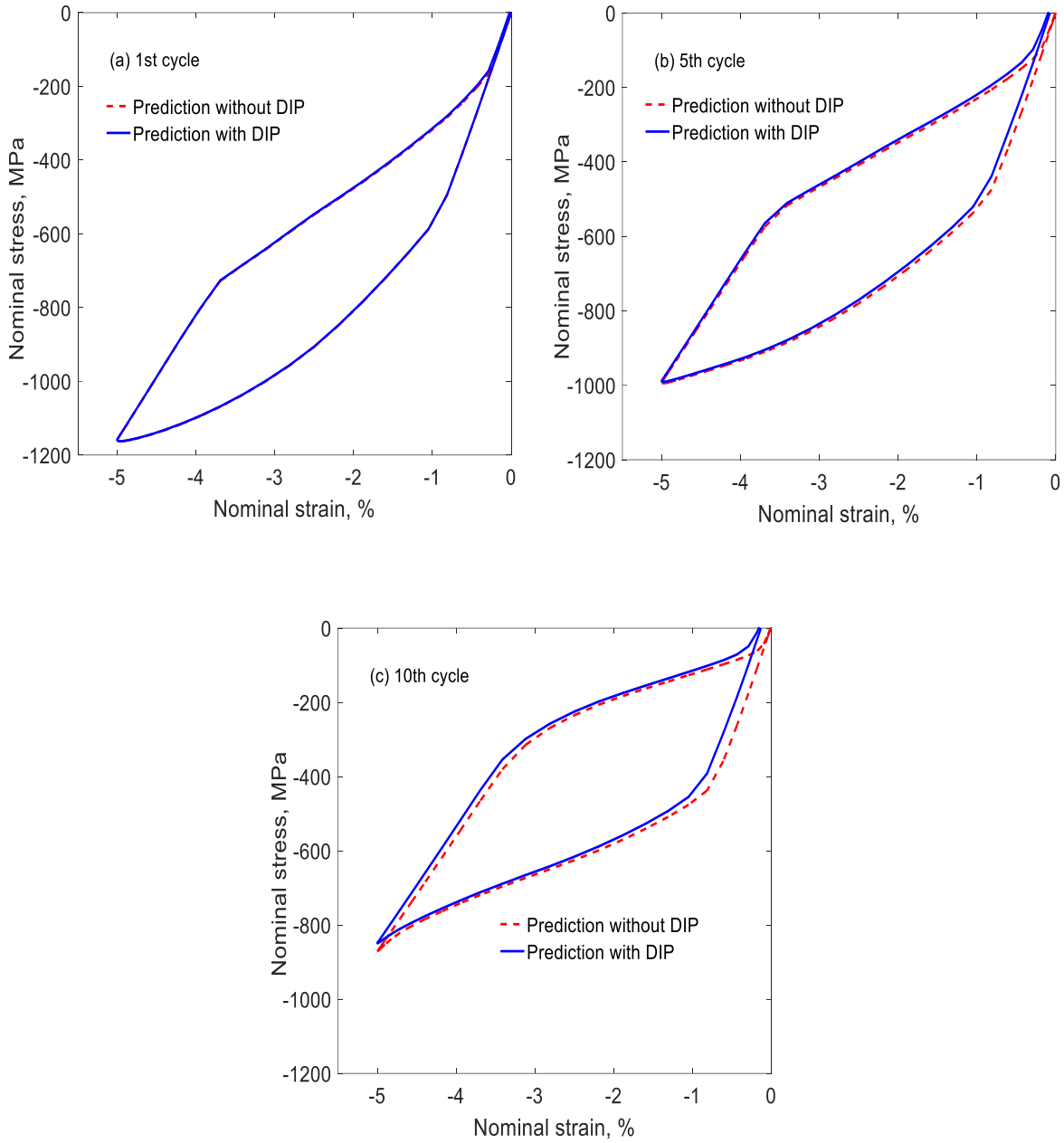

Fig. 9. Stress-strain diagram of NiTi SMA under compressive cyclic loading with a minimum strain of -5% and unloading to zero stress, with and without considering the effect of detwinning-induced plasticity: a) cycle 1, (b) cycle 5, and (c) cycle 10

As shown in Fig. 9, the effect of detwinning-induced plasticity in the first cycle is negligible but is more pronounced with increasing number of cycles. Similar to the results presented by Ebrahimi et al. [32], considering the effect of DIP reduces the absolute value of the maximum stress and increases the absolute value of the residual strain in the strain-controlled cyclic loading of NiTi SMA.

The contour plots of shearing deformation caused by detwinning-induced plasticity for two variants of martensite are depicted in Fig. 10

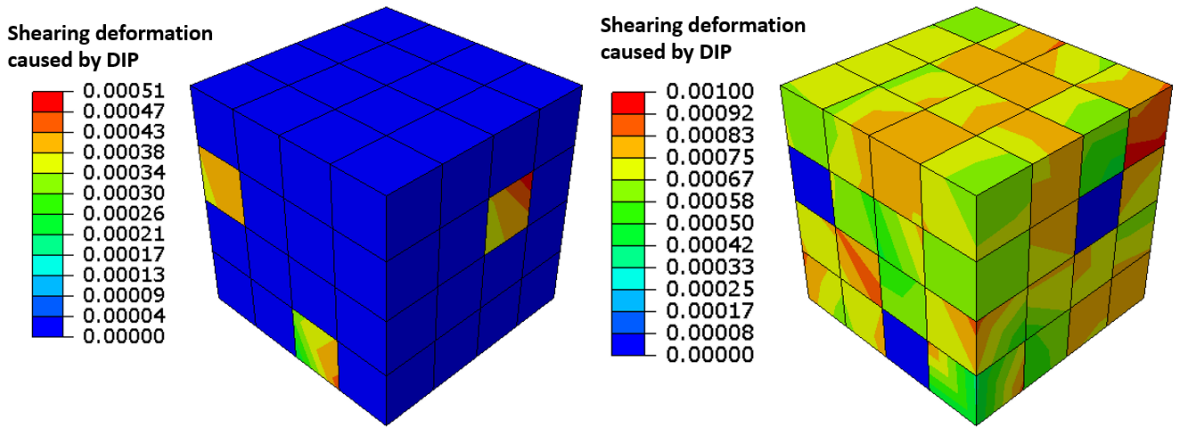

Fig. 10. contour plots of shearing deformation caused by detwinning-induced plasticity in two variants of martensite.

5. Conclusions

In this study a microstructure-based model for NiTi SMAs is developed by incorporating transformation-induced plasticity (TRIP), detwinning-induced plasticity (DIP), and accumulation of residual martensite into a finite-deformation crystal plasticity framework. The constitutive model is constructed at the single-crystal scale and also includes phase transformation and detwinning mechanisms. Using a proposed Helmholtz free energy, the driving forces for inelastic mechanisms are derived within the framework of thermodynamics. The constitutive model has been implemented in the Abaqus/Explicit finite-element program, using VUMAT subroutine to simulate a polycrystalline material. Considering various orientations for crystals, the effect of texture on tension-compression asymmetry is investigated. It is shown that different textures may cause harder, softer, or similar response in compression compared to tension, which is in good agreement with the comments of Gall and Sehitoglu [43], Gao et al. [44], and Thamburaja and Anand [15].

Due to the incorporation of the effect of residual martensite, the model provides accurate predictions of experimentally measured residual strain [15]. The incorporation of the inelastic DIP and TRIP deformation mechanisms and using appropriate form of free energy is shown to accurately capture the key features related to cyclic loading, including decrease in start stress

of austenite to martensite transformation, decrease in width of the hysteresis loop, and saturation of residual strain [38]. Finally, the effect of detwinning-induced plasticity in compressive cyclic loading of NiTi SMA is investigated. In strain-controlled cyclic compression-unloading tests DIP leads to a less negative peak stress and a more negative residual strain following several loading cycles [32]. Future applications of the model should include analysis of the inelastic deformation mechanisms such as DIP on the behavior of stents during crimping and deployment, including detailed 3D crystal plasticity modelling [45] of the role of grain boundaries on residual martensite and DIP concentrations. Additionally, future studies should incorporate DIP and TRIP into microstructure based fatigue indication parameters [46,47]. Fatigue failure remains a significant clinical problem for NiTi stents [48] and the analysis presented in the current study and the role of inelastic microstructural mechanisms in cyclic response of SMAs can potentially be used to guide the material and structural design of next-generation stents.

References

[1] N.B. Morgan, Medical shape memory alloy applications—the market and its products, Mater. Sci. Eng. A. 378 (2004) 16–23.

[2] L. Petrini, F. Migliavacca, Biomedical applications of shape memory alloys, J. Metall. 2011 (2011).

[3] W. Coral, C. Rossi, O.M. Curet, D. Castro, Design and assessment of a flexible fish robot actuated by shape memory alloys, Bioinspir. Biomim. 13 (2018) 56009.

[4] Y. Furuya, H. Shimada, Shape memory actuators for robotic applications, Mater. Des. 12 (1991) 21–28.

[5] D.J. Hartl, D.C. Lagoudas, Aerospace applications of shape memory alloys, Proc. Inst. Mech. Eng. Part G J. Aerosp. Eng. 221 (2007) 535–552.

[6] O. Benafan, M.R. Moholt, M. Bass, J.H. Mabe, D.E. Nicholson, F.T. Calkins, Recent Advancements in Rotary Shape Memory Alloy Actuators for Aeronautics, Shape Mem. Superelasticity. 5 (2019) 415–428.

[7] E. Williams, M.H. Elahinia, An automotive SMA mirror actuator: modeling, design, and experimental evaluation, J. Intell. Mater. Syst. Struct. 19 (2008) 1425–1434.

[8] D.C. Lagoudas, Shape Memory Alloys: Modeling and Engineering Applications, Springer, 2008.

[9] F. Auricchio, A. Reali, U. Stefanelli, A three-dimensional model describing stress-induced solid phase transformation with permanent inelasticity, Int. J. Plast. 23 (2007) 207–226.

[10] D. Lagoudas, D. Hartl, Y. Chemisky, L. Machado, P. Popov, Constitutive model for the numerical analysis of phase transformation in polycrystalline shape memory alloys, Int. J. Plast. 32 (2012) 155–183.

[11] M. Panico, L.C. Brinson, A three-dimensional phenomenological model for martensite reorientation in shape memory alloys, J. Mech. Phys. Solids. 55 (2007) 2491–2511.

[12] W. Zaki, Z. Moumni, A three-dimensional model of the thermomechanical behavior of shape memory alloys, J. Mech. Phys. Solids. 55 (2007) 2455–2490.

[13] J. Arghavani, F. Auricchio, R. Naghdabadi, A. Reali, S. Sohrabpour, A 3-D phenomenological constitutive model for shape memory alloys under multiaxial loadings, Int. J. Plast. 26 (2010) 976–991.

[14] L. Xu, T. Baxevanis, D.C. Lagoudas, A three-dimensional constitutive model for the martensitic transformation in polycrystalline shape memory alloys under large deformation, Smart Mater. Struct. 28 (2019) 74004.

[15] P. Thamburaja, L. Anand, Polycrystalline shape-memory materials: effect of crystallographic texture, J. Mech. Phys. Solids. 49 (2001) 709–737.

[16] P. Thamburaja, L. Anand, Superelastic behavior in tension–torsion of an initially-textured Ti–Ni shape-memory alloy, Int. J. Plast. 18 (2002) 1607–1617.

[17] P. Thamburaja, L. Anand, Thermo-mechanically coupled superelastic response of initially-textured Ti-Ni sheet, Acta Mater. 51 (2003) 325–338.

[18] L. Anand, M.E. Gurtin, Thermal effects in the superelasticity of crystalline shape-memory materials, J. Mech. Phys. Solids. 51 (2003) 1015–1058.

[19] P. Thamburaja, Constitutive equations for martensitic reorientation and detwinning in shape-memory alloys, J. Mech. Phys. Solids. 53 (2005) 825–856.

[20] P. Thamburaja, H. Pan, F.S. Chau, Martensitic reorientation and shape-memory effect in initially textured polycrystalline Ti–Ni sheet, Acta Mater. 53 (2005) 3821–3831.

[21] X.M. Wang, B.X. Xu, Z.F. Yue, Micromechanical modelling of the effect of plastic deformation on the mechanical behaviour in pseudoelastic shape memory alloys, Int. J. Plast. 24 (2008) 1307–1332.

[22] S. Manchiraju, P.M. Anderson, Coupling between martensitic phase transformations and plasticity: A microstructure-based finite element model, Int. J. Plast. 26 (2010) 1508–1526.

[23] C. Yu, G. Kang, D. Song, Q. Kan, Effect of Martensite Reorientation and Reorientation-induced plasticity on Multiaxial Transformation Ratchetting of Super-elastic NiTi Shape Memory Alloy: New Consideration in Constitutive Model, Int. J. Plast. (2015).

[24] C. Yu, G. Kang, Q. Kan, Crystal plasticity based constitutive model of NiTi shape memory alloy considering different mechanisms of inelastic deformation, Int. J. Plast. 54 (2014) 132–162.

[25] C. Yu, G. Kang, Q. Kan, D. Song, A micromechanical constitutive model based on crystal plasticity for thermo-mechanical cyclic deformation of NiTi shape memory alloys, Int. J. Plast. 44 (2013) 161–191.

[26] C. Yu, G. Kang, D. Song, Q. Kan, Micromechanical constitutive model considering plasticity for super-elastic NiTi shape memory alloy, Comput. Mater. Sci. 56 (2012) 1–5.

[27] Y. Xiao, P. Zeng, L. Lei, Micromechanical modeling on thermomechanical coupling of cyclically deformed superelastic NiTi shape memory alloy, Int. J. Plast. 107 (2018) 164–188.

[28] S. Dhala, S. Mishra, A. Tewari, A. Alankar, Modeling of finite deformation of pseudoelastic NiTi shape memory alloy considering various inelasticity mechanisms, Int. J. Plast. 115 (2019) 216–237.

[29] G. Kang, Q. Kan, L. Qian, Y. Liu, Ratchetting deformation of super-elastic and shape-memory NiTi alloys, Mech. Mater. 41 (2009) 139–153.

[30] D.C. Lagoudas, P.B. Entchev, Modeling of transformation-induced plasticity and its effect on the behavior of porous shape memory alloys. Part I: constitutive model for fully dense SMAs, Mech. Mater. 36 (2004) 865–892.

[31] Y. Liu, Z. Xie, J. Van Humbeeck, L. Delaey, Asymmetry of stress–strain curves under tension and compression for NiTi shape memory alloys, Acta Mater. 46 (1998) 4325–4338.

[32] P. Ebrahimi, J. Arghavani, R. Naghdabadi, J.P. McGarry, On the effect of detwinning-induced plasticity in compressive cyclic loading of NiTi shape memory alloys, Mech. Mater. 148 (2020).

[33] V.A. Lubarda, Constitutive theories based on the multiplicative decomposition of deformation gradient: Thermoelasticity, elastoplasticity, and biomechanics, Appl. Mech. Rev. 57 (2004) 95–108.

[34] V. Fohrmeister, G. Díaz, J. Mosler, Classic crystal plasticity theory vs crystal plasticity theory based on strong discontinuities—Theoretical and algorithmic aspects, Int. J. Numer. Methods Eng. 117 (2019) 1283–1303.

[35] H. Erdle, T. Böhlke, A gradient crystal plasticity theory for large deformations with a discontinuous accumulated plastic slip, Comput. Mech. 60 (2017) 923–942.

[36] G. Rengarajan, K.R. Rajagopal, On the form for the plastic velocity gradient Lp in crystal plasticity, Math. Mech. Solids. 6 (2001) 471–480. https://doi.org/10.1177/108128650100600501.

[37] E. Patoor, D.C. Lagoudas, P.B. Entchev, L.C. Brinson, X. Gao, Shape memory alloys, Part I: General properties and modeling of single crystals, Mech. Mater. 38 (2006) 391–429.

[38] D. Song, G. Kang, Q. Kan, C. Yu, C. Zhang, The effect of martensite plasticity on the cyclic deformation of super-elastic NiTi shape memory alloy, Smart Mater. Struct. 23 (2014) 15008.

[39] M. Jamal, S. Jalali Asadabadi, I. Ahmad, H.A.R. Aliabad, Elastic constants of cubic crystals, Comput. Mater. Sci. 95 (2014) 592–599. https://doi.org/10.1016/j.commatsci.2014.08.027.

[40] T.M. Brill, S. Mittelbach, W. Assmus, M. Mullner, B. Luthi, Elastic properties of NiTi, J. Phys. Condens. Matter. 3 (1991) 9621–9627. https://www.academia.edu/17345671/Elastic_properties_of_NiTi (accessed June 23, 2020).

[41] K. Gall, H. Sehitoglu, R. Anderson, I. Karaman, Y.I. Chumlyakov, I. V Kireeva, On the mechanical behavior of single crystal NiTi shape memory alloys and related polycrystalline phenomenon, Mater. Sci. Eng. A. 317 (2001) 85–92. http://www.scopus.com/inward/record.url?eid=2-s2.0-0035980536&partnerID=40&md5=e077f11118a2a3e7b466665c6283c6cb.

[42] D. Depriester, Computing Euler angles with Bunge convention from rotation matrix, (2018). https://doi.org/10.13140/RG.2.2.34498.48321/4.

[43] K. Gall, H. Sehitoglu, Role of texture in tension-compression asymmetry in polycrystalline NiTi, Int. J. Plast. 15 (1999) 69–92. https://doi.org/10.1016/S0749-6419(98)00060-6.

[44] X. Gao, M. Huang, L.C. Brinson, Multivariant micromechanical model for SMAs. Part 1. Crystallographic issues for single crystal model, Int. J. Plast. 16 (2000) 1345–1369. https://doi.org/10.1016/S0749-6419(00)00013-9.

[45] J.P. McGarry, B.P. O'Donnell, P.E. McHugh, E. O'Cearbhaill, R.M. McMeeking, Computational examination of the effect of material lnhomogeneity on the necking of stent struts under tensile loading, J. Appl. Mech. Trans. ASME. 74 (2007) 978–989. https://doi.org/10.1115/1.2722776.

[46] O.J. McCarthy, J.P. McGarry, S.B. Leen, The effect of grain orientation on fretting fatigue plasticity and life prediction, Tribol. Int. 76 (2014) 100–115. https://doi.org/10.1016/j.triboint.2013.09.023.

[47] O.J. McCarthy, J.P. McGarry, S.B. Leen, Micro-mechanical modelling of fretting fatigue crack initiation and wear in Ti-6Al-4V, Int. J. Fatigue. 62 (2014) 180–193. https://doi.org/10.1016/j.ijfatigue.2013.04.019.

[48] D. Scheinert, S. Scheinert, J. Sax, C. Piorkowski, S. Bräunlich, M. Ulrich, G. Biamino, A. Schmidt, Prevalence and clinical impact of stent fractures after femoropopliteal stenting, J. Am. Coll. Cardiol. 45 (2005) 312–315. https://doi.org/10.1016/j.jacc.2004.11.026.

Appendix

Table A.1: Crystallographic data for the 24 martensite variants in NiTi shape memory alloy [21]

α	m_1^α	m_2^α	m_3^α	b_1^α	b_2^α	b_3^α
1	-0.8889	-0.4044	0.2152	0.4114	-0.4981	0.7633
2	-0.4044	-0.8889	-0.2152	-0.4981	0.4114	-0.7633
3	0.8889	0.4044	0.2152	-0.4114	0.4981	0.7633
4	0.4044	0.8889	-0.2152	0.4981	-0.4114	-0.7633
5	-0.8889	0.4044	-0.2152	0.4114	0.4981	-0.7633
6	0.4044	-0.8889	0.2152	0.4981	0.4114	0.7633
7	0.8889	-0.4044	-0.2152	-0.4114	-0.4981	-0.7633
8	-0.4044	0.8889	0.2152	-0.4981	-0.4114	0.7633
9	0.2152	0.8889	0.4044	0.7633	-0.4114	0.4981
10	0.2152	-0.8889	-0.4044	0.7633	0.4114	-0.4981
11	-0.2152	-0.4044	-0.8889	-0.7633	-0.4981	0.4114
12	-0.2152	0.4044	0.8889	-0.7633	0.4981	-0.4114
13	-0.2152	0.8889	-0.4044	-0.7633	-0.4114	-0.4981
14	-0.2152	-0.8889	0.4044	-0.7633	0.4114	0.4981
15	0.2152	0.4044	-0.8889	0.7633	0.4981	0.4114
16	0.2152	-0.4044	0.8889	0.7633	-0.4981	-0.4114
17	0.8889	-0.2152	0.4044	-0.4114	-0.7633	0.4981
18	-0.8889	-0.2152	-0.4044	0.4114	-0.7633	-0.4981
19	0.4044	0.2152	0.8889	0.4981	0.7633	-0.4114
20	-0.4044	0.2152	-0.8889	-0.4981	0.7633	0.4114
21	0.8889	0.2152	-0.4044	-0.4114	0.7633	-0.4981
22	-0.8889	0.2152	0.4044	0.4114	0.7633	0.4981
23	-0.4044	-0.2152	0.8889	-0.4981	-0.7633	-0.4114
24	0.4044	-0.2152	-0.8889	0.4981	-0.7633	0.4114

Table A.2: Crystallographic data for martensite detwinning systems in NiTi shape memory alloy [20]

α	w_1^α	w_2^α	w_3^α	a_1^α	a_2^α	a_3^α
1	-0.5846	0	0.8133	0	0.2804	0
2	0	-0.5846	-0.8133	0.2804	0	0
3	-0.5846	0	-0.8133	0	0.2804	0
4	0	-0.5846	0.8133	0.2804	0	0
5	-0.5846	0	-0.8133	0	0.2804	0
6	0	-0.5846	0.8133	0.2804	0	0
7	-0.5846	0	0.8133	0	0.2804	0
8	0	-0.5846	-0.8133	0.2804	0	0
9	-0.8133	-0.5846	0	0	0	0.2804
10	-0.8133	0.5846	0	0	0	0.2804
11	-0.8133	0	-0.5846	0	0.2804	0
12	-0.8133	0	0.5846	0	0.2804	0
13	-0.8133	0.5846	0	0	0	0.2804
14	-0.8133	-0.5846	0	0	0	0.2804
15	-0.8133	0	0.5846	0	0.2804	0
16	-0.8133	0	-0.5846	0	0.2804	0
17	0.5846	-0.8133	0	0	0	0.2804
18	-0.5846	-0.8133	0	0	0	0.2804
19	0	-0.8133	-0.5846	0.2804	0	0
20	0	-0.8133	0.5846	0.2804	0	0
21	-0.5846	-0.8133	0	0	0	0.2804
22	0.5846	-0.8133	0	0	0	0.2804
23	0	-0.8133	0.5846	0.2804	0	0
24	0	-0.8133	-0.5846	0.2804	0	0